International Journal of Precision Engineering and Manufacturing-Green Technology (2023) 10:1263–1280
https://doi.org/10.1007/s40684-022-00491-3
Online ISSN 2198-0810
Print ISSN 2288-6206

REGULAR PAPER

Multi-mode Soft Composite Bending Actuators Based on Glass fiber Textiles Interwoven with Shape Memory Alloy Wires: Development and use in the Preparation of Soft Grippers

Oybek Valijonovich Tuyboyov[1] · **Geo-Sung Lee**[2] · **Gil-Yong Lee**[1,2]

Received: 25 August 2022 / Revised: 12 November 2022 / Accepted: 18 November 2022 / Published online: 15 December 2022

Abstract

We develop multi-mode soft composite bending actuators based on glass fiber textiles interwoven with shape memory alloy (SMA) wires and a soft matrix of polydimethylsiloxane. We describe their detailed design and fabrication. We varied the interweaving patterns of SMA wires, such that the actuators exhibit multi-mode bending behaviors. Actuators with three different bending modes were fabricated, and their performances were evaluated in terms of curvature. We varied the stiffness of glass fiber textiles and the diameters of SMA wires. Bidirectional multi-mode actuations were achieved when SMA wires of different interwoven patterns were combined with glass fiber textiles. We present prototypes of such actuators and demonstrate their actuations. Finally, we prepared gripper prototypes using these actuators; they grasped different objects according to bending mode. Our technique will aid the development of soft robotics, as well as other scientific and engineering applications.

Keywords Soft composite · Multi–mode bending actuator · Shape memory alloy (SMA) · Soft gripper

1 Introduction

There is considerable demand for low-cost, lightweight, adaptable, and intelligent systems [1, 2]. Shape memory alloys (SMAs) have applications in flexible, adaptable, soft, and lightweight systems [3, 4], as well as the automotive [5], biomedical [6–8], soft robotics [9–13], and aerospace [14, 15] fields. Among the many forms of SMAs, wires can readily be integrated into various structures [16, 17]; are cost-effective and lightweight; and create useful actuating forces during axial contraction [18, 19]. SMA wires can easily be integrated into textile or fiber reinforcements during the preparation of composite structures and wearable devices [5, 20–23]. These features of SMA wires render them useful when preparing soft actuators [5, 13, 17, 19, 22, 24–27]. Several examples of such works include soft-morphing structures based on a woven smart soft composite [27]; SMA tendon-based soft robotic actuators [25]; a soft finger with embedded SMA wires [13]; and SMA-based smart soft composite structure that can bend and twist [26]. Such actuators have many applications in soft grippers and soft robotics [12, 25, 28–33]. Most previous works focused on single actuation modes (bending or twisting) induced by SMA wires within a soft actuator. Although several SMA wire-based, multi-mode soft actuators have been proposed [24, 26, 34], the soft robotic applications of such multi-mode soft actuators have received limited attention; this topic is challenging but merits investigation. Here, we present multi-mode bending actuators fabricated using glass fiber textiles interwoven with SMA wires within a soft matrix of polydimethylsiloxane (PDMS). We detail the design and fabrication of actuators with three different bending modes. We vary the stiffness of the glass fiber textile and the diameter of the SMA wire. We evaluate actuation performance in terms of bending deformation (curvature). We also fabricate multi-mode and bidirectionally bending prototypes, then present their actuating motions. Finally, we fabricate soft gripper prototypes with multi-mode bending actuators that grasp objects using different bending modes.

✉ Gil-Yong Lee
gylee@kumoh.ac.kr

[1] Department of Mechanical Engineering, Kumoh National Institute of Technology, Gyeongbuk, Gumi 39177, Republic of Korea

[2] Department of Aeronautics, Mechanical and Electronic Convergence Engineering , Kumoh National Institute of Technology , Gyeongbuk, Gumi 39177, Republic of Korea

2 Design and Fabrication of Multi-Mode Soft Composite Bending Actuators

2.1 Actuator Design

Figure 1(a) shows a schematic of a multi-mode bending actuator fabricated from a woven glass fiber textile, an interwoven SMA wire, and a soft matrix (PDMS). We varied the interweaving patterns of the wire; the resulting actuators are denoted as Types 1–3 in Fig. 1(b-d). In Type-1 actuators, the SMA wires are oriented eccentric to the neutral axis, and the direction of eccentricity does not change longitudinally along the beam axis [Fig. 1(b)]. In Type-2 actuators, the SMA wire is interwoven such that the direction of the eccentric plane changes once along the beam axis, at the halfway point of the beam [Fig. 1(c)]. In a Type-3 actuator, the direction of the eccentric plane of the wire changes twice, at one-third and two-thirds of the length of the beam [Fig. 1(d)]. When the SMA wire is heated, it contracts longitudinally, generating axial compressive stresses that induce the first bending mode of the Type-1 actuator, the second bending mode of the Type-2 actuator, and the third bending mode of the Type-3 actuator. Schematics of these actuation modes are presented in Fig. 1(b–d).

2.2 Fabrication of Multi-Mode Soft Composite Bending Actuators

Figure 2 shows fabrication schematics. After a woven glass fiber textile is prepared [Fig. 2(a)], the SMA wire is interwoven with the textile [Fig. 2(b)] in a Type-1, -2, or -3 pattern; the construct is placed in a mold [Fig. 2(c)]; and the soft matrix (PDMS) is added. Molding and curing [Fig. 2(d)] yield a soft composite actuator [Fig. 2(e)]. We used two different grades (denoted by T20 and T40) of glass fiber threads to weave the textiles [inset in Fig. 2(a)]. To prepare T20/T40 threads, 20/40 glass fiber yarns were bundled using a stepper motor [see the Materials and Supplementary Figure S1(a, b)]. We weaved both threads with the textile; the moduli of the soft composite exhibited variation. Supplementary Figure S2(a, c, e) shows scanning electron microscope images of the glass fiber yarn as purchased, along with T20 and T40 threads. Corresponding schematics are shown in Supplementary Figure S2(b, d).

As shown in Fig. 3(a), we used a custom loom (fabricated by a three-dimensional printer) to weave the glass fiber threads (T20 and T40). The warp threads were placed in the loom, and the weft threads were woven by a needle onto the loom [Fig. 3(a)]. Supplementary Figure S1(c–g) provides more detailed information regarding the weaving processes and the glass fiber textiles that were fabricated using T20 and T40 threads. We used five warp threads for all specimens. The glass fiber textiles woven with T20/T40 threads were approximately 7/8 mm in width and 1.2/1.4 mm in

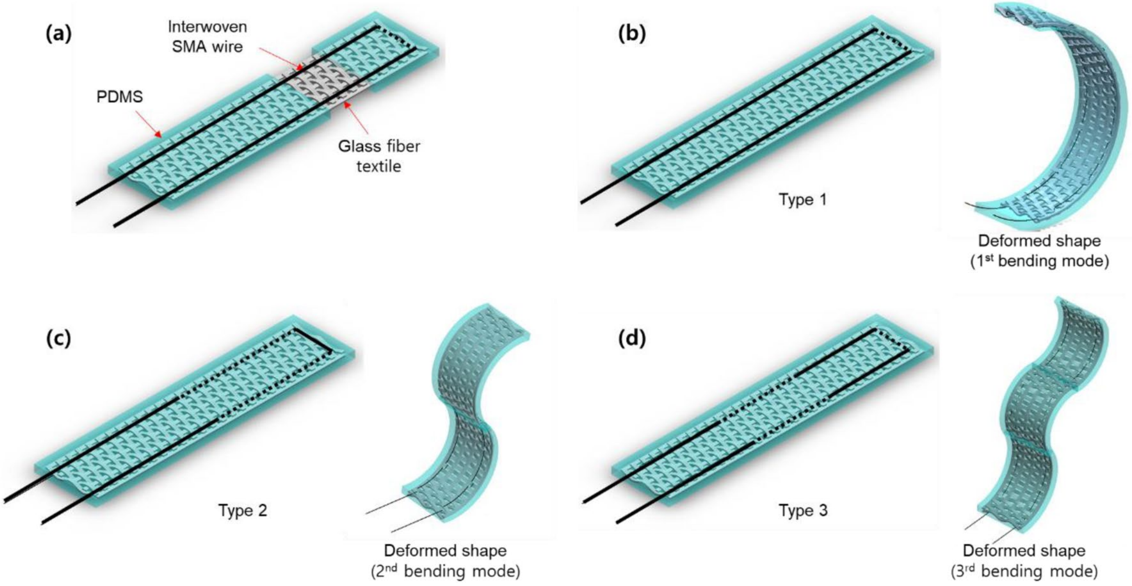

Fig. 1 Schematics of multi-mode soft composite bending actuators based on glass fiber textiles interwoven with shape memory alloy (SMA) wires. **a** Schematic of a soft composite bending actuator. Schematics of **b** Type-1, **c** -2, and **d** -3 actuators and their actuation modes (i.e., first, second, and third bending modes) for different interweavings of SMA wire

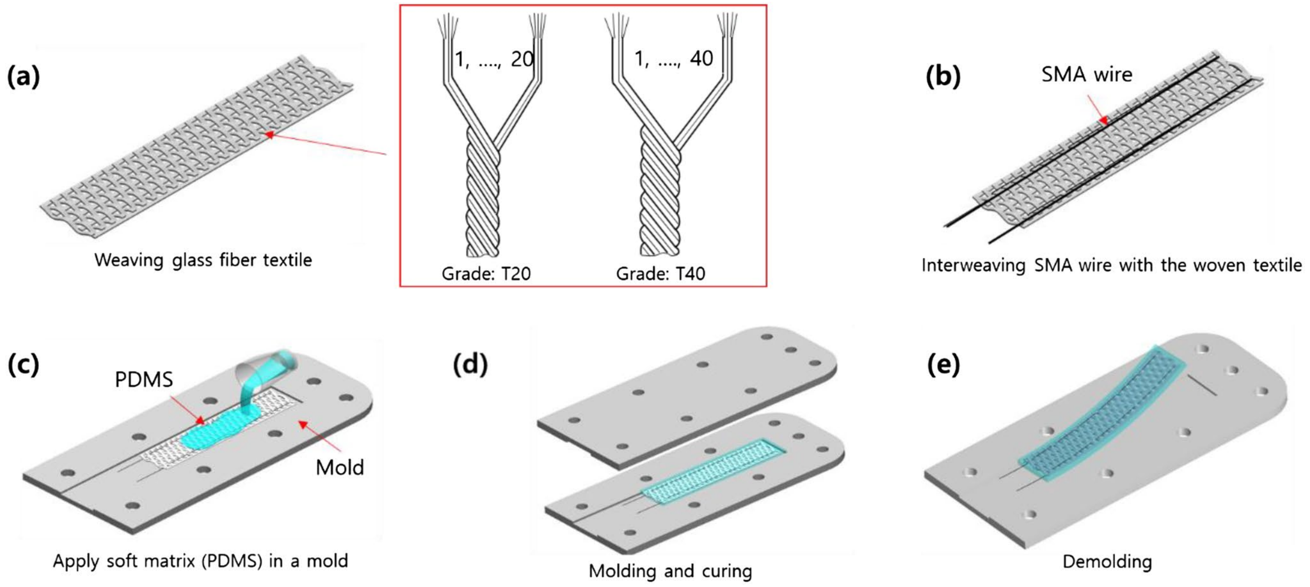

Fig. 2 Schematic of soft composite bending actuator fabrication. **a** The woven glass fiber textile. **b** SMA wire interwoven into the textile. **c** PDMS applied in a mold. Each specimen was prepared via **d** molding and curing and **e** demolding

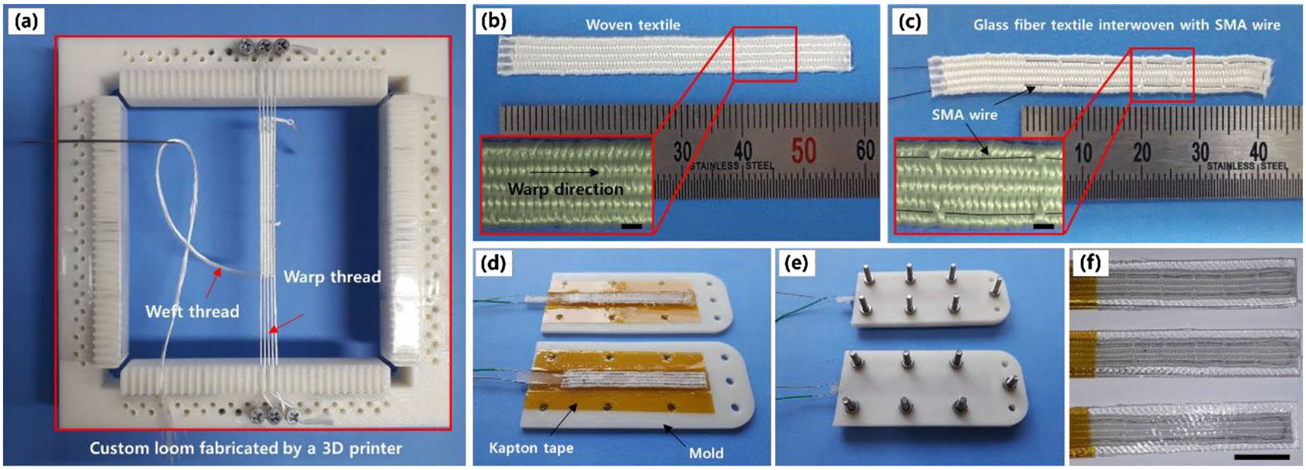

Fig. 3 Stepwise fabrication of a soft composite actuator. **a** After placement of warp threads (T20 and T40) in a custom loom fabricated by a three-dimensional printer, the weft threads were woven to form base textiles. **b** The textiles were tailored and **c** interwoven with SMA wires. **d**, **e** PDMS was added to the molds and cured. **f** Optical images of the final specimens. Insets in (**b**, **c**): Magnified images of the tailored woven textiles and SMA wire-interwoven glass fiber textiles. Scale bars: 1 mm for insets in (**b**, **c**); 10 mm for (**f**)

thickness, with small variations (approximately ± 0.5 mm). We prepared woven glass fiber textiles 50–60 mm in length [Supplementary Figure S1(f–g)]. Regarding exterior dimensions of the prepared woven glass fiber textiles, we designed the size of the soft composite actuator as 10 mm wide, 1.5 mm thick, and 40 mm long. The number of weft threads was approximately 120/40 mm (3/mm) for the textile with T20 threads and 70/40 mm (1.75/mm) for the textile with T40 threads. The optical microscope images in Supplementary Figure S1(h, i) show the number of weft threads per millimeter. The glass fiber warp and weft threads were identical. The warp threads were tightly held on the loom (under tension) during weaving; the flying weft threads were held less tightly. Thus, the weft threads appear thicker than the warp threads in Fig. 3(a). To ensure even weaves, we applied a comb after each weft thread had been woven. Figure 3(b) shows a tailored glass fiber textile after weaving; the inset in Fig. 3(b) and Supplementary Figure S1(f–i) reveal nearly even weaving patterns along the warp direction. As shown in Fig. 3(c), SMA wire was interwoven into the glass fiber textile shown in Fig. 3(b) and placed in a mold with PDMS [Fig. 3(d)]. Kapton tape was applied to the mold

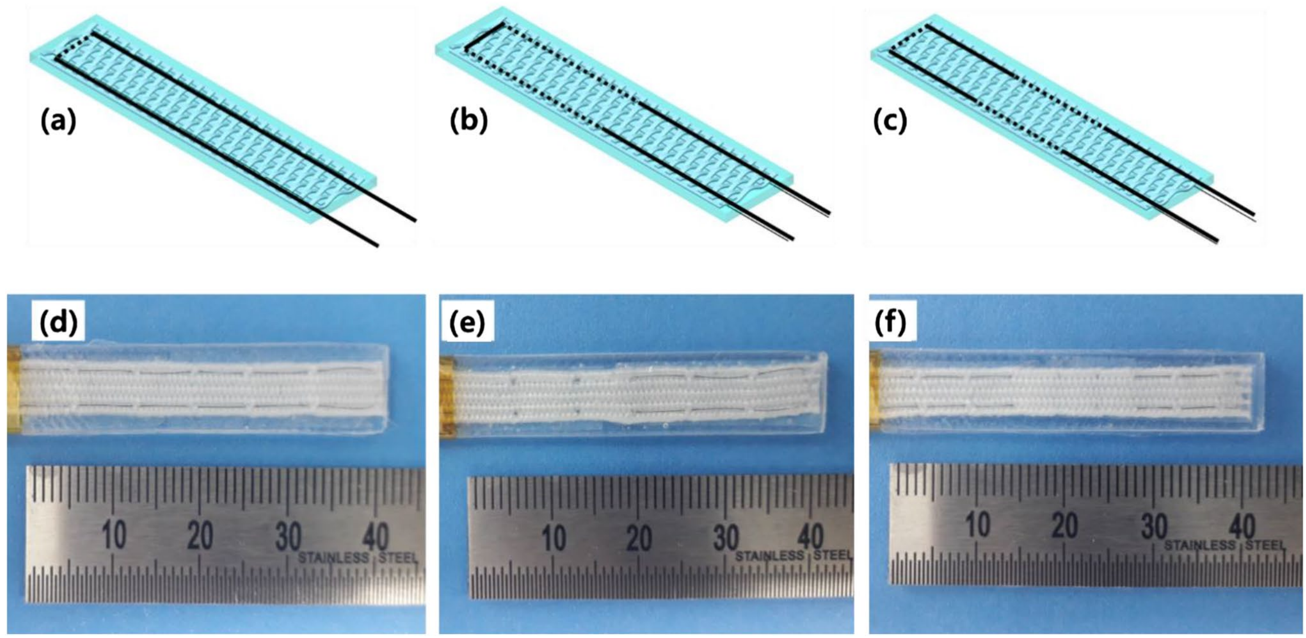

Fig. 4 **a**–**c** Schematics and **d**–**f** photographs of Type-1, -2, and - 3 soft composite actuators

Table 1 Soft composite actuators with varying SMA wire interweaving patterns

SMA wire interweaving pattern	Grade (Glass fiber thread)	SMA wire diameter d_{SMA} (μm)
Type-1	T20	100
Type-2	T20	100
Type-3	T20	100

Table 2 Soft composite actuators with varying grades of glass fiber thread used for the base textiles and varying diameters of interwoven SMA wires

SMA wire interweaving pattern	Grade (Glass fiber thread)	SMA wire diameter d_{SMA} (μm)
Type-2	T20	100
Type-2	T40	100
Type-2	T20	150
Type-2	T40	150

surface for easy demolding. Curing [Fig. 3(e)] yielded the final composite actuators [Fig. 3(f)]; Type-1 specimens are shown in Fig. 3(f). Supplementary Figure S3 provides additional details concerning the fabrication of soft composite actuators.

Figure 4 shows representative Type-1, -2, and -3 actuators fabricated as described above. First, we varied only the interweaving patterns of SMA wires with same thread grade and SMA wire diameter. Table 1 summarizes the glass fiber thread grades and the SMA wire diameters. To investigate the effects of the soft composite modulus and the SMA wire diameter, we fabricated Type-2 soft actuators with different glass fiber threads for the base textile, along with different SMA wire diameters (Table 2); this approach simplified the experiments.

Supplementary Figure S4(a–c) shows photographs of the fabricated soft actuators listed in Table 1; Supplementary Figure S4(d–f) shows photographs of the fabricated soft actuators listed in Table 2. The Type-2 actuator with T20 threads and a 100-μm-diameter SMA wire in the first row of Table 2 is identical to the specimen in the second row of Table 1.

2.3 Bending Deformations of Multi-Mode Soft Composite Bending Actuators

Figure 5(a) assumes that the SMA wire generates a uniform compressive force (F_{SMA}) along the length of a bent beam of eccentricity e, neglecting the axial strain along the length. The curvature ρ and the radius of curvature R of the bent actuator are then simply described by Eq. (1) [25]:

$$\rho = \frac{1}{R} = \frac{F_{SMA}e}{EI} = \frac{M_B}{EI} \tag{1}$$

where E is Young's modulus, I is the area moment of inertia of the soft composite, and M_B is the equivalent bending

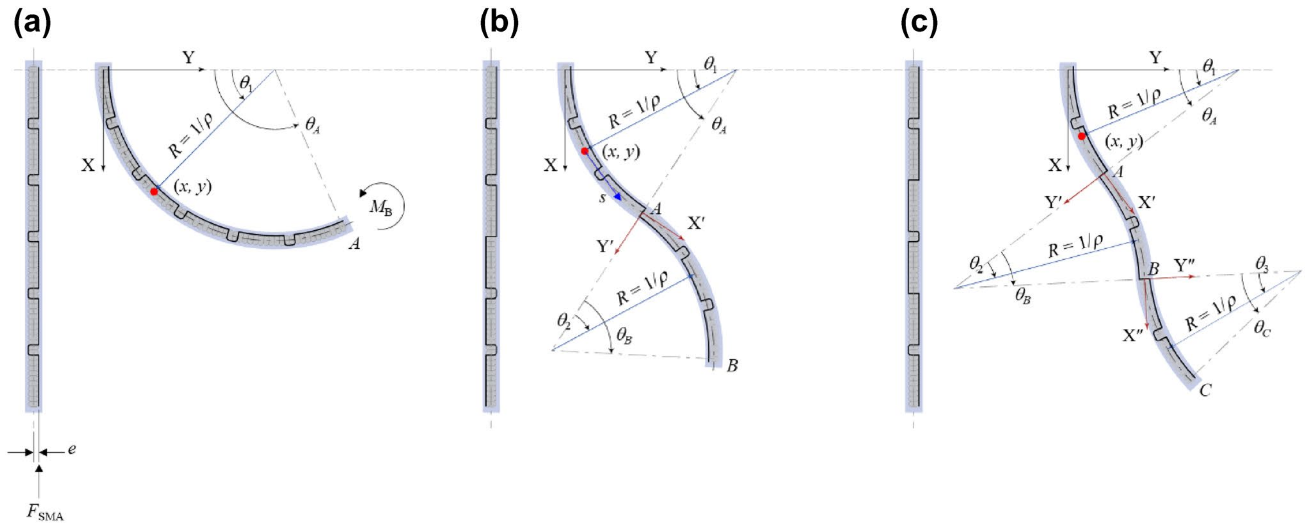

Fig. 5 Schematics of actuator bending deformations for different SMA wire interweavings: **a** Type-1, **b** Type-2, and **c** Type-3

moment. The position $[x\ y]^{\mathrm{T}}$ on the bent beam is then expressed by:

$$\begin{bmatrix} x \\ y \end{bmatrix} = \begin{bmatrix} R\sin\theta_1 \\ R(1-\cos\theta_1) \end{bmatrix} \quad \text{where,}\quad 0 \le \theta_1 \le \theta_A = \frac{L}{R} \tag{2}$$

where θ_A is the bending angle [25, 38].

We obtain a similar expression for position $[x\ y]^{\mathrm{T}}$ on the bent beam for a Type-2 soft bending actuator [Fig. 5(b)]:

$$\begin{bmatrix} x \\ y \end{bmatrix} = \begin{cases} \begin{bmatrix} R\sin\theta_1 \\ R(1-\cos\theta_1) \end{bmatrix} & \text{for}\ \ 0 \le \theta_1 \le \theta_A = \dfrac{L}{2R} \\ \begin{bmatrix} x_A \\ y_A \end{bmatrix} + [T_R(\theta_A)]\,[T_M] \begin{bmatrix} R\sin\theta_2 \\ R(1-\cos\theta_2) \end{bmatrix} & \text{for}\ \ 0 \le \theta_2 \le \theta_B = \dfrac{L}{2R} \end{cases} \tag{3}$$

where $\begin{bmatrix} x_A \\ y_A \end{bmatrix} = \begin{bmatrix} R\sin\theta_A \\ R(1-\cos\theta_A) \end{bmatrix}$

$[T_R(q_A)]$ and $[T_M]$ are the coordinate transform matrices described by:

$$[T_R(\theta_A)] = \begin{bmatrix} \cos\theta_A & -\sin\theta_A \\ \sin\theta_A & \cos\theta_A \end{bmatrix} \quad \text{and} \quad [T_M] = \begin{bmatrix} 1 & 0 \\ 0 & -1 \end{bmatrix} \tag{4}$$

We assume that the bending actuator assumes similar radius of curvature (but opposite bending direction) along s, which is a coordinate acquired along the deflection curve of the bent beam.

For a Type-3 soft bending actuator, the position $[x\ y]^{\mathrm{T}}$ on the bent beam is obtained as follows [see Fig. 5(c)]:

$$\begin{bmatrix} x \\ y \end{bmatrix} = \begin{cases} \begin{matrix} R\sin\theta_1 \\ R(1-\cos\theta_1) \end{matrix} & \text{for}\ \ 0 \le \theta_1 \le \theta_A = \dfrac{L}{3R} \\ \begin{bmatrix} x_A \\ y_A \end{bmatrix} + [T_R(\theta_A)]\,[T_M] \begin{bmatrix} R\sin\theta_2 \\ R(1-\cos\theta_2) \end{bmatrix} & \text{for}\ \ 0 \le \theta_2 \le \theta_B = \dfrac{L}{3R} \\ \begin{bmatrix} x_B \\ y_B \end{bmatrix} + [T_R(\theta_A-\theta_B)] \begin{bmatrix} R\sin\theta_3 \\ R(1-\cos\theta_3) \end{bmatrix} & \text{for}\ \ 0 \le \theta_3 \le \theta_C = \dfrac{L}{3R} \end{cases} \tag{5}$$

where $\begin{bmatrix} x_A \\ y_A \end{bmatrix} = \begin{bmatrix} R\sin\theta_A \\ R(1-\cos\theta_A) \end{bmatrix}$ and $\begin{bmatrix} x_B \\ y_B \end{bmatrix} = \begin{bmatrix} R\sin\theta_A \\ R(1-\cos\theta_A) \end{bmatrix} + [T_R(\theta_A)]\,[T_M] \begin{bmatrix} R\sin\theta_B \\ R(1-\cos\theta_B) \end{bmatrix}$

We experimentally extracted the positions of the bent beams and fitted the data to Eqs. (2), (3), and (5) for Type-1, -2, and -3 actuators, respectively, using the fitting coefficient $\rho = 1/R$. The equivalent bending moments (M_{B} values) were estimated by Eq. (1) using the fitting coefficient $\rho = 1/R$.

2.4 Moduli of Soft Composites

We prepared specimens for tensile tests of soft composites based on T20 and T40 glass fiber threads [Supplementary Figure S5(a, b)]; pure PDMS specimens were also prepared [Supplementary Figure S5(c)]. As shown in Supplementary Figure S5(d), the Young's moduli of the T20 and T40 soft composites were estimated via linear fitting of the stress-strain responses of the tensile specimens; the estimated moduli of the T20 and T40 composites were $E_{\mathrm{T20}} = 19.5299$ MPa and $E_{\mathrm{T40}} = 36.7098$ MPa, respectively. The Young's modulus of PDMS was 0.2032 MPa [Supplementary Figure S5(e)]. We used the experimental values of the moduli to fit the models, then estimate the curvatures and bending moments of the actuators described above. Note that PDMS viscoelasticity may affect the dynamic behaviors of soft composite actuators; however, we assumed that this influence could be ignored because the PDMS modulus is small compared with the moduli of soft composites. Although the moduli of soft composites are dominated by the glass fiber textiles, PDMS helps maintain the exterior dimensions, thus supporting longitudinal compression; it provides the elastic force that restores the bending deformations of the composites upon cooling [12, 35]. PDMS also protects the woven structures from environmental or other damage [35].

3 Performance Evaluation of Multi-Mode Soft Composite Bending Actuators

3.1 Characterization of Bending Behaviors

The experimental setup included a camera, a current driver, a data acquisition board, and a personal computer. This setup was used to characterize the bending behaviors of the actuators (Fig. 6). Step currents from 100 to 500 mA were applied to each specimen for 10 s, using the custom-built current driver and a data acquisition system (National Instruments cDAQ-9174 with the 9205 and 9264 modules) controlled by the personal computer. Upon application of the step current, the camera captured the lateral bending (deflection) of each actuator.

Figure 7(a–c) shows the bending deflections of representative specimens (Type-1, -2, and -3) at various input currents. The images in Fig. 7(a–c) were acquired 10 s after step current application (100 to 500 mA). The glass fiber thread grades and SMA wire diameters are listed in Table 1. As shown in Fig. 7(a–c), bending deformation was not obvious up to 200 mA, implying that the resistive heat applied was inadequate to initiate the temperature-induced phase transformation of SMA wire [4, 36, 37]. As the current increased to 300 mA, the actuators began to bend. At a current of 500 mA, we observed noticeable bending deflections in all actuators. These were evaluated in terms of bending curvatures (see Sect. 2.3). Supplementary Movie S1 depicts the motions of Type-1, -2, and -3 actuators when the current was 500 mA.

We extracted the positions of the bent actuators using image processes (MATLAB). First, images obtained 10 s after the application of specific step currents were loaded into MATLAB and trimmed using a predefined window (300×225 pixels) to ensure that each image included only the beam. After each image had been converted to grayscale, we identified the pixels $[x_{\text{pix},i}\ y_{\text{pix},i}]^{\mathrm{T}}$ at which the value was maximal (i.e., at the white portions of beams evident against the black backgrounds) along both horizontal and vertical scans; $i = 1, 2, 3, \ldots, N$ are the indices of the resulting pixels. These pixels $[x_{\text{pix},i}\ y_{\text{pix},i}]^{\mathrm{T}}$ were converted to displacements using the relationship $[x_i\ y_i]^{\mathrm{T}} = a[x_{\text{pix},i}\ y_{\text{pix},i}]^{\mathrm{T}}$, where a is a conversion factor (here, $a = 0.2$ mm/pixel). The positional data $[x_i\ y_i]^{\mathrm{T}}$ were fitted to the $[x\ y]^{\mathrm{T}}$ values obtained using Eqs. (2), (3), and (5) to iteratively identify the best fitting coefficient ρ, which minimized the normalized error r, defined as:

$$r = \sum_{i=1}^{N} \frac{1}{N} \sqrt{\frac{(x - x_i)^2 + (y - y_i)^2}{L^2}} \tag{6}$$

where N is the number of data points obtained from the image and L is the length of the beam (here, 40 mm).

The extracted position data $[x_i\ y_i]^{\mathrm{T}}$ for interwoven Type-1, -2, and -3 SMA wires are plotted in Fig. 8(a–c) for step currents from 100 to 500 mA; the grayscale images of the bent beams and the model-fitted deflection curves are also plotted. As shown in Fig. 8, the deflections of the bent beams closely fitted the model (i.e., the deflections were adequately defined by the bending curvature ρ).

Figure 9(a) compares the curvatures of the bent actuators in terms of step input currents for various interwoven SMA wire patterns. We also calculated the bending moments (M_{B}

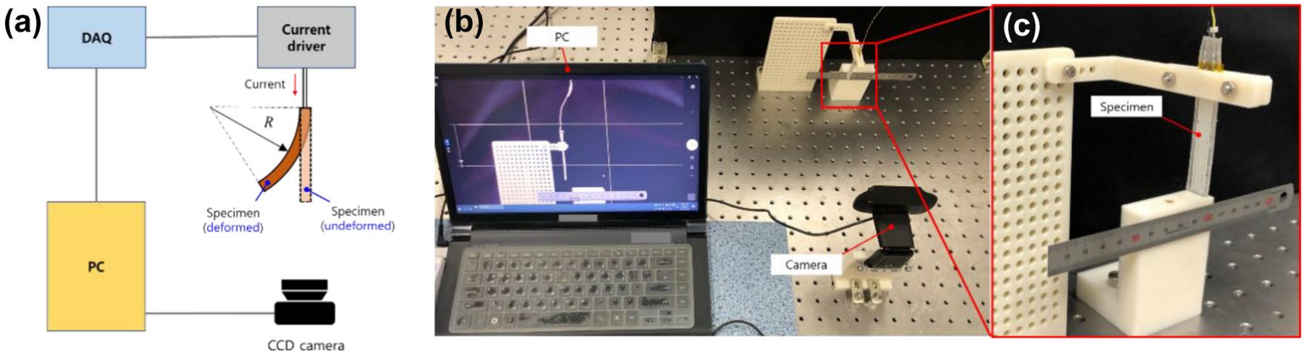

Fig. 6 **a** Schematic and **b** photograph of the experimental setup. **c** Magnified image of the setup near the specimen

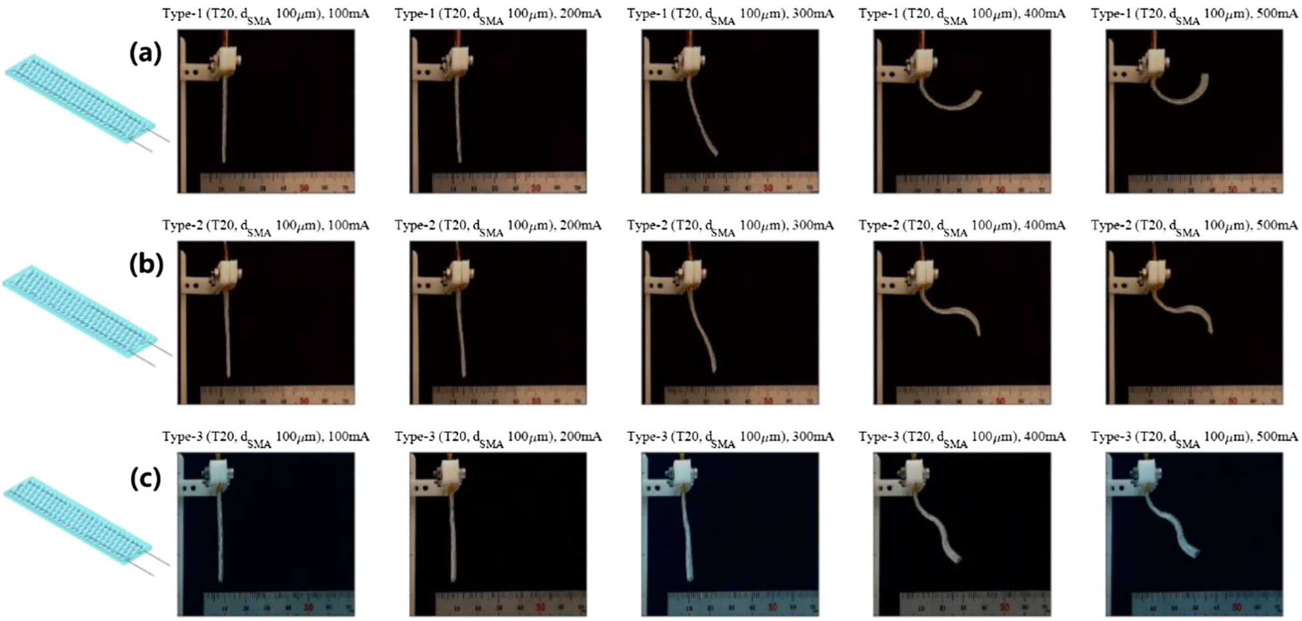

Fig. 7 Responses of soft actuators as the step input currents ranged from 100 to 500 mA (captured 10 s after currents were applied) for different SMA wire interweavings: **a** Type-1, **b** Type-2, and **c** Type-3

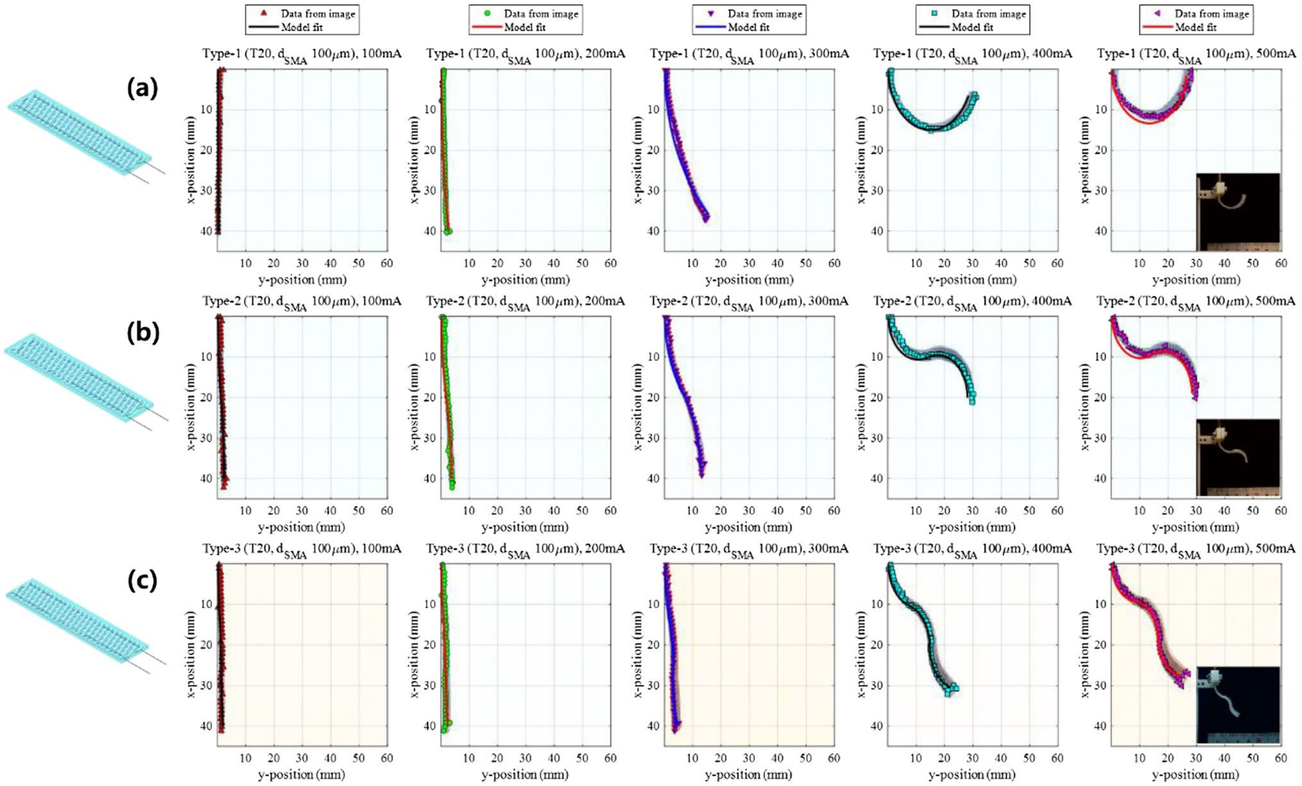

Fig. 8 Positional data for **a** Type-1, **b** Type-2, and **c** Type-3 soft actuators obtained by image processes and model fitting at various step currents (100 to 500 mA)

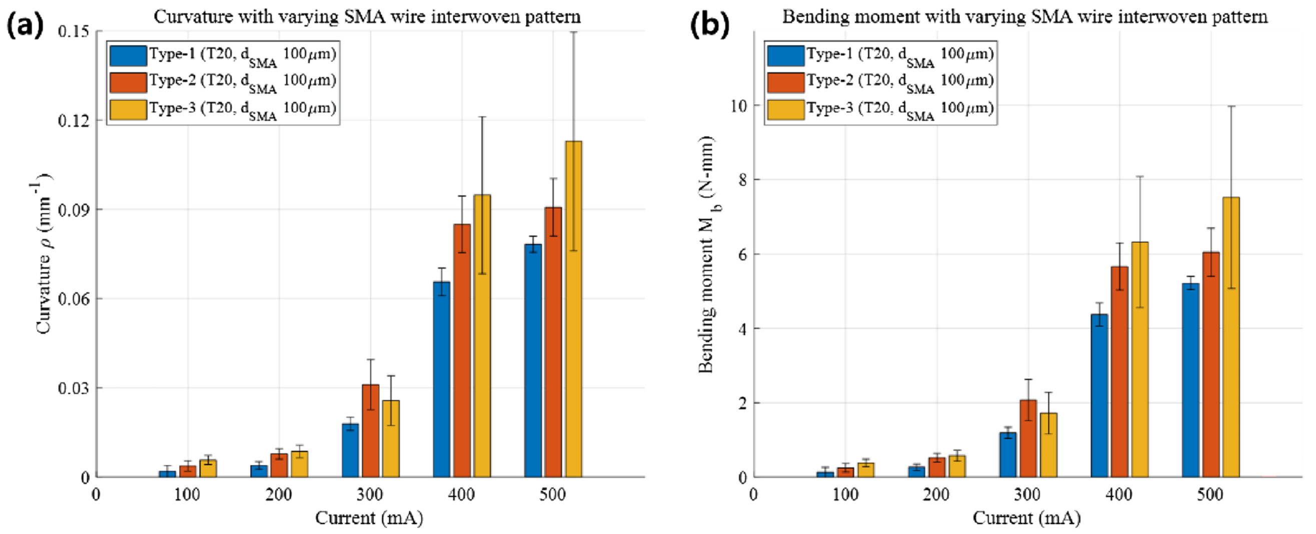

Fig. 9 **a** Curvatures and **b** bending moments of soft composite actuators as the SMA wire interweavings and step currents varied

values) of the actuators using Eq. (1); we plot the estimated moments according to the varying step currents for various interwoven SMA wire patterns in Fig. 9(b). The mean curvatures estimated by the model for the Type-1, -2, and -3 actuators (at 500 mA) were 0.079, 0.091, and 0.11 mm^{-1}, respectively; the corresponding mean estimated bending moments at 500 mA were 5.22, 6.04, and 7.52 N·mm. Note that the variations are acceptable, reflecting possible imprecisions in the dimensions of the fabricated actuators; variations in the SMA wire eccentricity e; and possible variations in interwoven actuator qualities that can be attributed to imperfect fabrication. The Type-2 and -3 actuator data exhibit more errors, compared with the Type-1 actuator data, presumably because the more complex SMA wire interweavings of the Type-2 and -3 actuators create more dimensional errors during fabrication.

The maximum bending angle (θ_A) of the actuator was 178.8° at a length of 40 mm (Type-1) and a step current of 500 mA. This performance is comparable with the performances of a composite using an SMA wire-nylon-glass fiber textile (200°; 86 mm length at 800 mA) [34]; a bio-inspired shape memory alloy composite actuator (180°; 150 mm length at 600 mA) [19]; an SMA-fiber-reinforced plastic-based soft actuator (58°; 70 mm length at 3 A) [38]; a textile-reinforced soft actuator (270°; 195 mm length at 1.5 A) [39]; and a soft actuator using a free-sliding SMA wire tendon (400°; 100 mm length at 950 mA) [25]. In terms of the curvature $\rho = \theta/L$ (where θ is the bending angle and L is the length of the bending actuator), the maximum curvature achieved by our soft actuator (0.079 mm^{-1} for Type-1 actuator) is better than the maximum curvatures of a shape memory composite using an SMA wire-nylon-glass fiber textile (0.041 mm^{-1}) [34]; a bio-inspired shape memory alloy composite actuator (0.021 mm^{-1}) [19]; an SMA-fiber-reinforced plastic-based soft actuator (0.015 mm^{-1}) [38]; and a textile-reinforced soft actuator (0.024 mm^{-1}) [39], and is similar with a soft actuator using a free-sliding SMA wire tendon (0.07 mm^{-1}) [25]. The similar soft actuators in previous studies [19, 25, 34, 38, 39] principally explored the first bending mode induced by SMA wire; our actuators are configured using different bending modes. The other bending mode actuations (Types-2 and -3) also exhibited large bending curvatures (0.091 mm^{-1} for Type-2 and 0.11 mm^{-1} for Type-3) and bending angles (104.3° for Type-2 and 84.0° for Type-3), comparable with the bending curvatures in previous studies [19, 25, 34, 38, 39].

Next, we investigated actuator bending behaviors according to the grade of textile thread and the diameter of the interwoven SMA wire; Table 2 summarizes information regarding actuators fabricated using different thread grades and SMA wire diameters. The specimens used for experiments are shown in Supplementary Figure S4(a) and (d–f). See Supplementary Figures S1 and S3 for details concerning how specimens were prepared.

Figure 10(a–d) shows the bending deflections of representative actuators fabricated using different thread grades and SMA wires of different diameters. The images were captured 10 s after application of the step current (100 to 500 mA). Supplementary Movie S2 captures the motions of the actuators (at a step current of 500 mA) as the textile grade and SMA wire diameter were varied. The positional data ($[x_i\ y_i]^T$ values) for actuators with different thread grades and SMA wire diameters were extracted as described above, then plotted for step currents from 100 to 500 mA (Fig. 11).

As the thread grade increased from T20 to T40, the larger modulus of the soft composite reduced actuator deflection

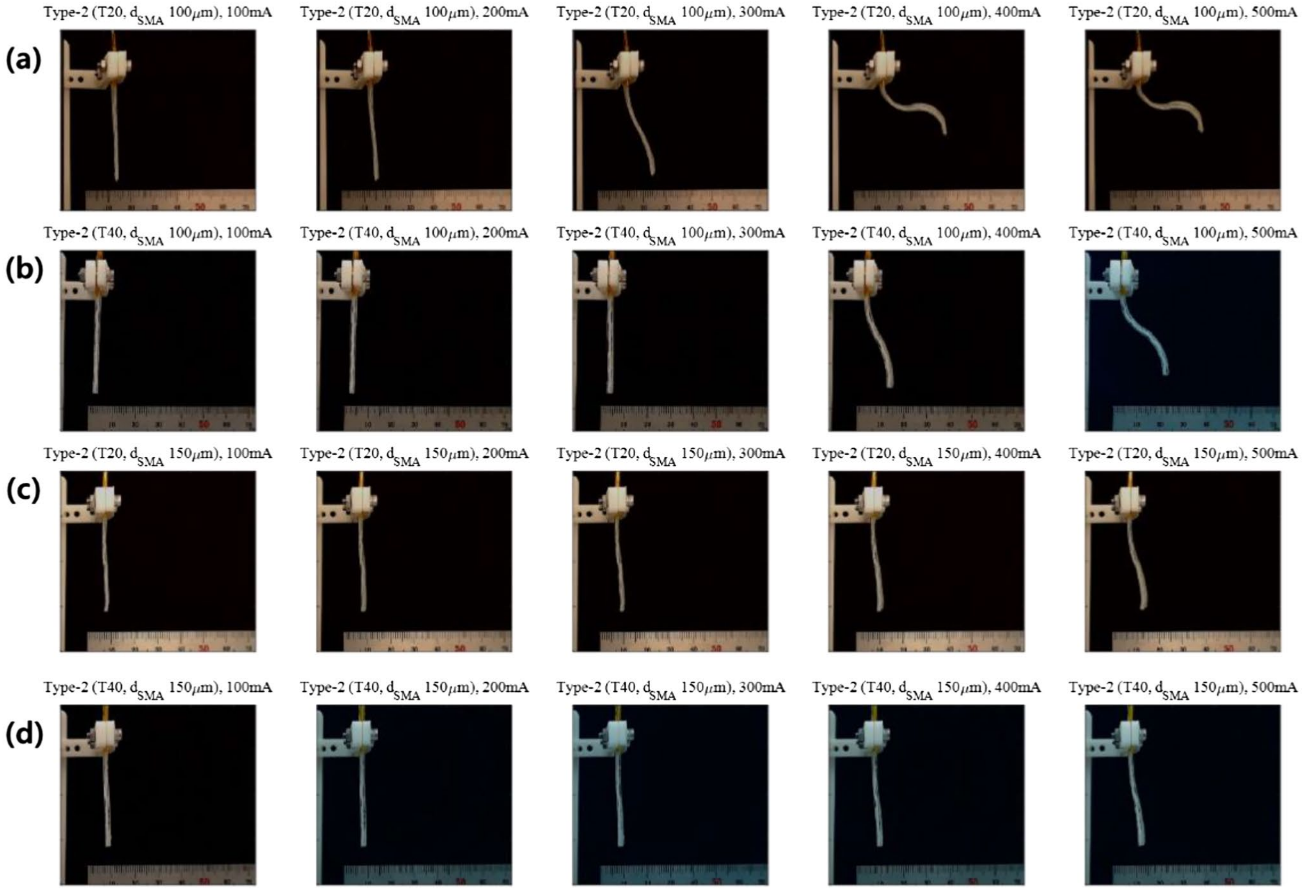

Fig. 10 Responses of soft actuators with different grades of glass fiber thread (T20 and T40) of the base textile and different interwoven SMA wire diameters (d_{SMA}). **a** T20, d_{SMA} 100 µm; **b** T40, d_{SMA} 100 µm; **c** T20, d_{SMA} 150 µm; **d** T40, d_{SMA} 150 µm

at the same input current, comparing Fig. 11(a) and (b) for 100-µm-diameter SMA wire; and comparing Fig. 11(c) and (d) for 150-µm-diameter SMA wire. As shown in Fig. 11(a, b) and Fig. 11(c, d), actuators fabricated using thicker SMA wire (150 µm) exhibited less deflection compared with actuators fabricated using thinner SMA wire (100 µm) at all tested input currents. The input power reflects the temperature change in SMA wire [40]. The equation is $P = {I_{SMA}}^2 R_{SMA} = mc(dT/dt)$, where P is the power input to the SMA wire, I_{SMA} is the current, R_{SMA} is the electrical resistance of the wire, m is the wire mass, c is the wire specific heat capacity, and T and t are the temperature and time, respectively. In this equation, $R_{SMA} = \rho_e L/A$, $m = \rho_d AL$, and $A = (\pi/4)(d_{SMA})^2$. Using these parameters, the following equation is generated:

$$\frac{dT}{dt} = \frac{\rho_e}{\rho_d c}\left(\frac{4}{\pi}\right)^2 \frac{1}{d_{SMA}^4} I_{SMA}^2 \qquad (7)$$

In Eq. (7), ρ_e and ρ_d are the electrical resistivity and density of the SMA wire, respectively; L is the wire length; A is the cross-sectional area; and d_{SMA} is the wire diameter. Equation (7) indicates that as the SMA wire becomes thicker (i.e., d_{SMA} becomes larger), the temperature change over time (dT/dt) decreases for a specific input current I_{SMA}; this calculation assumes that the material properties of the SMA wire do not substantially vary during temperature-induced phase transformations. According to Eq. (7), a soft actuator fabricated using thicker SMA wire (150 µm) would be expected to exhibit less deflection than an actuator fabricated using thinner SMA wire (100 µm) at all input currents because of slower changes in temperature (dT/dt). However, as indicated by Eq. (7), bending deformation can be enhanced by delivery of more current to a soft actuator with a thicker SMA wire (150 µm) [see Supplementary Movie S3, which captures the bending deformations of soft actuators (T20 and T40 weaves with 150-µm SMA wires) during larger input currents (700 mA)].

Figure12 plots the estimated curvatures and bending moments of actuators that differ in terms of thread grade and SMA wire diameter with variations in step input currents.

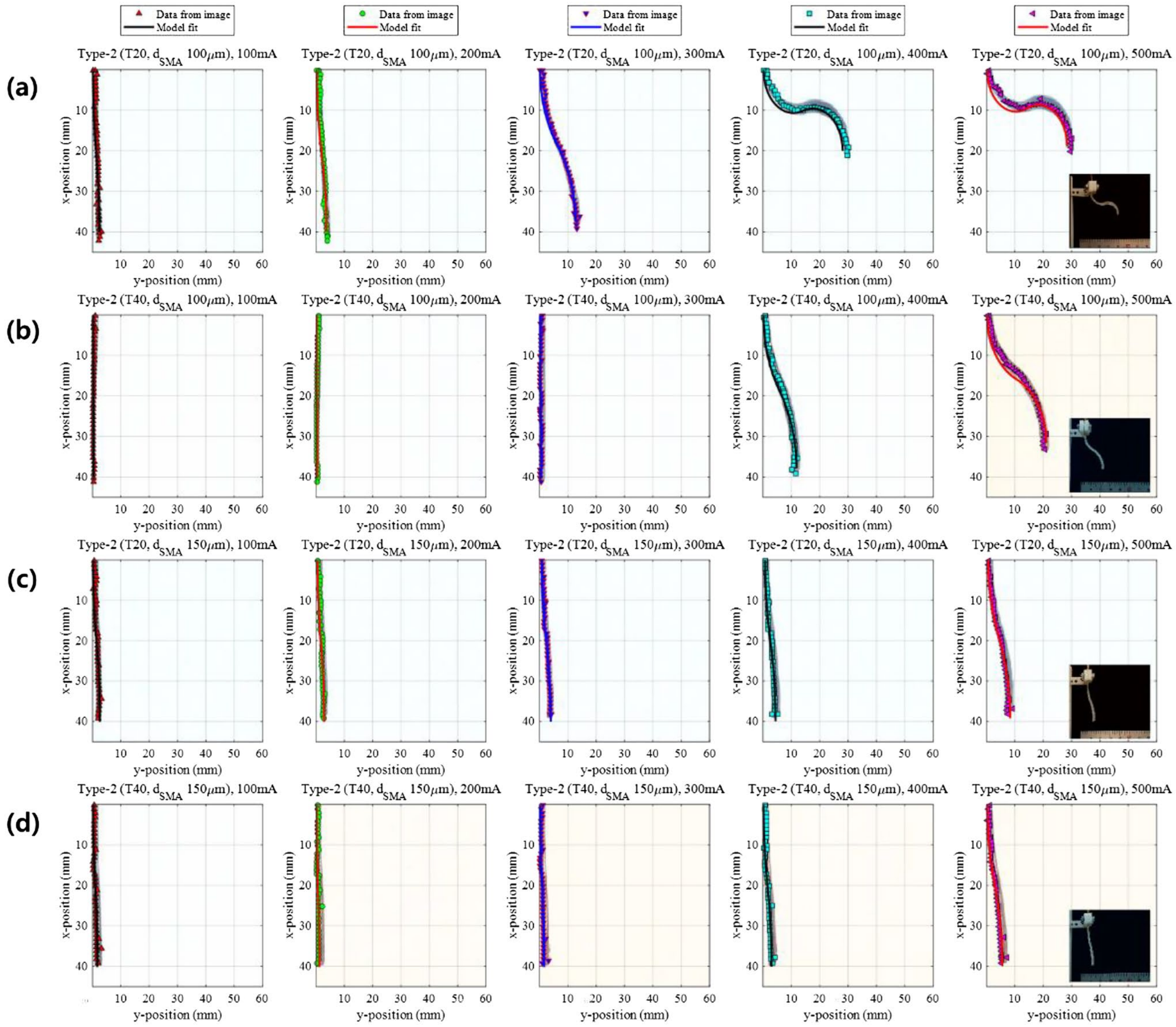

Fig. 11 Positional data for soft actuators obtained by image processes and model fitting at various step currents (100 to 500 mA) and for different glass fiber thread grades and SMA wire diameters. **a** T20, d_{SMA} 100 µm; **b** T40, d_{SMA} 100 µm; **c** T20, d_{SMA} 150 µm; **d** T40, d_{SMA} 150 µm

As the thread grade increases to T40 for an actuator with an SMA wire 100 µm in diameter, the mean curvature decreases to approximately 67.0% (0.061 mm^{-1} at 500 mA) compared with the mean curvature of a soft actuator with T20 threads (0.091 mm^{-1} at 500 mA). For a soft actuator with 150-µm-diameter SMA wire, the reduction is approximately 38.5% (0.015 mm^{-1} at 500 mA) compared with the mean curvature of an actuator with T20 threads (0.039 mm^{-1} at 500 mA).

In terms of the modulus ratio of actuators with T20 and T40 threads ($E_{\mathrm{T20}}/E_{\mathrm{T40}}$ is approximately 0.532 in our experiments), Eq. (1) indicates that the curvature decreases by 53.2% when an actuator that contains T40 threads is compared with an actuator that contains T20 threads. Considering quality variations among fabricated actuators, the experimental results exhibit good agreement with the simple bending model [Eq. (1)]; the differences are approximately within ± 15%. Similarly, the experimental and theoretical bending deformations of the actuators (in terms of SMA wire diameter) exhibit reasonable agreement. Equation (7) indicates that the effect of a slower change in temperature (dT/dt) is 19.8% less for a soft actuator with 150-µm-diameter SMA wire than for a soft actuator with 100-µm-diameter SMA wire at the same input current. For actuators with T20 threads, as the SMA wire diameter increases to 150 µm, the mean curvature is approximately 42.9% (0.039 mm^{-1} at 500 mA) compared with the mean curvature of an actuator with 100-µm SMA wire

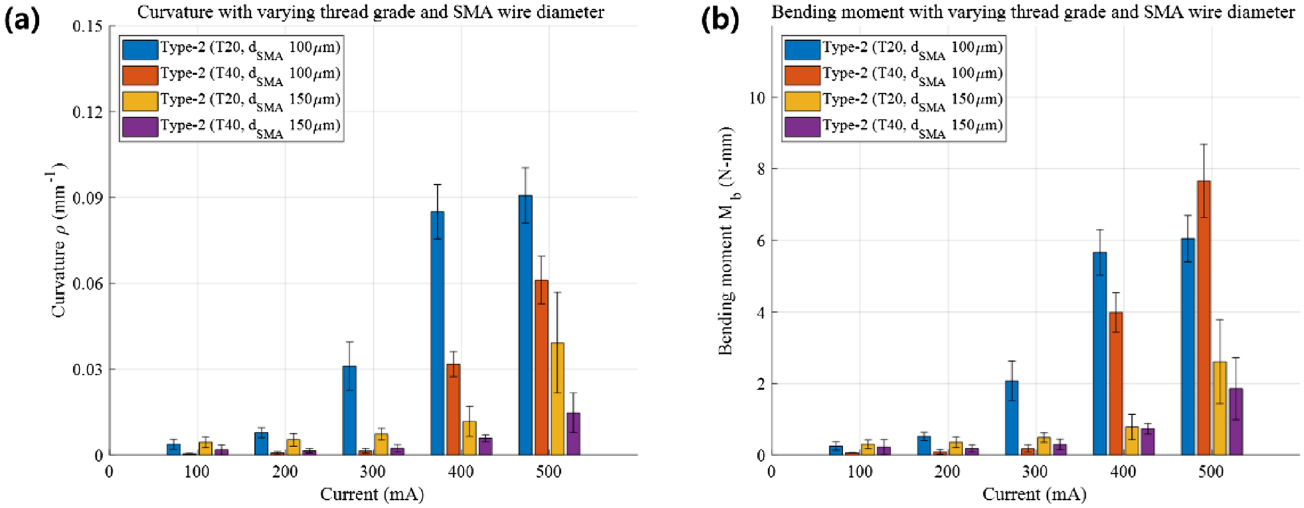

Fig. 12 **a** Curvatures and **b** bending moments of soft composite actuators with different thread grades and interwoven SMA wire diameters when the step currents varied

(0.091 mm^{-1} at 500 mA). For actuators with T40 threads, the value decreases to approximately 24.6% (0.015 mm^{-1} at 500 mA) compared with the mean curvature of an actuator with 100-µm SMA wire (0.061 mm^{-1} at 500 mA). The experimental data for actuators with T40 threads exhibit good agreement with the simple estimations provided by Eqs. (1) and (7); the difference is approximately 5%. However, the difference increases to approximately 20% for actuators with T20 threads, which can be attributed to quality issues with the fabricated specimens. The actuator curvature decreases as the modulus of the soft composite and the diameter of the SMA wire increase. The bending moments were estimated as similar values for soft actuators with the same SMA wire diameter at the same input current [Fig. 12(b)]. The simple models/estimations in the present study exhibit good agreement with the overall behavioral tendencies of the actuators. More precise predictive models should be derived in the future; these should consider the nonlinear and temperature-dependent mechanical properties of SMA wires [41, 42], as well as structural nonlinearity that can be attributed to the large actuator deflections [43].

3.2 Bidirectional Soft Composite Bending Actuators

SMA interweaving into a base textile can be extended to fabricate bidirectional and multi-mode bending actuators. An example is shown in Fig. 13(a, b). The prototype contains two SMA wires interwoven in the Type-1 pattern, but the wire orientations are reversed. The eccentricity directions of the outer wire [1; Fig. 13(a)] and the inner wire [2; Fig. 13(b)] are opposed; the actuator can be bidirectionally bent in the first bending mode upon application of current to both wires. Figure 13(c) captures temporal images of the bidirectional bending motions of the prototype induced via sequential activation of each SMA wire from $t=0$ to $t=8$ s. A 500-mA step current was applied to SMA wire 1 at $t=0$ s for 1 s; the input current applied to SMA wire 2 was zero. The resulting bending deformation (to the left) was captured at $t=1$ s. The input current to SMA wire 1 was zero, whereas a 500-mA step current was applied to SMA wire 2 at $t=1$ s for 1 s. The resulting bending deformation (to the right) was captured at $t=2$ s. The sequential applications of current to each SMA wire were repeated to $t=8$ s, and the resulting bending deformations are shown in Fig. 13(c). We present the timing of input currents to each wire in Fig. 13(d).

Another example of a bidirectionally bending actuator is shown in Fig. 14(a, b). This actuator contains two SMA wires (1 and 2) interwoven in the Type-2 pattern, and the orientations of the two wires are reversed. The directions of eccentricity of the outer SMA wire 1 and the inner SMA wire 2 are opposed [Fig. 14(a, b)] such that the actuator bends bidirectionally (in the second bending mode) upon application of current to both wires. Figure 14(c) captures the bidirectional bending motions upon sequential activation of each SMA wire from $t=0$ s to $t=8$ s. The current sequence was conducted as described above; the bending deformations are shown in Fig. 14(c). Figure 14(d) shows the input current times to each wire. The bidirectional actuators (Type-1 and -2) exhibited nearly symmetrical bending deformations in both directions over several cyclic actuations. Supplementary Movie S4 captures the actuating motions (Type-1 and -2) shown in Figs. 13(c) and 14(c).

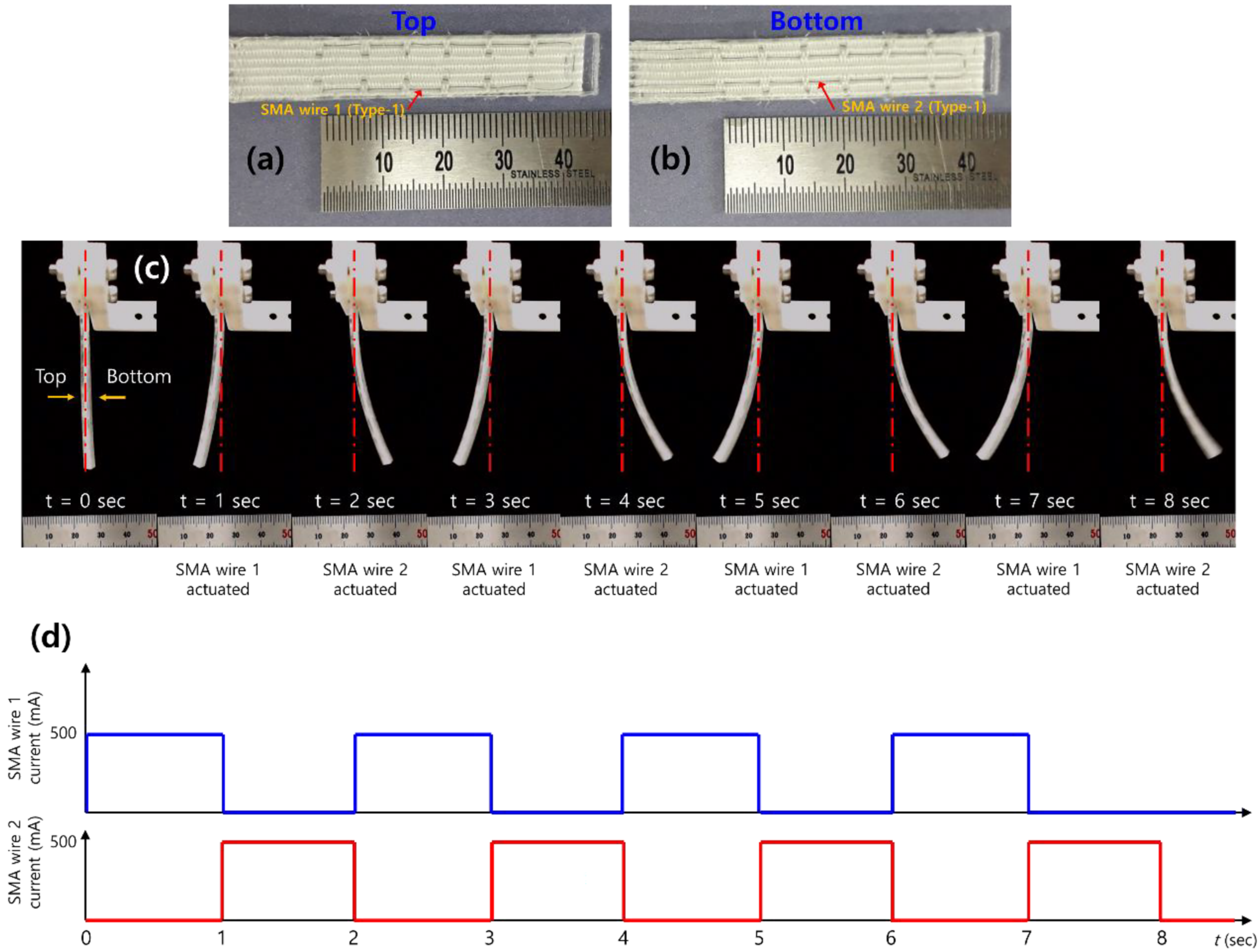

Fig. 13 **a**, **b** Optical images of a Type-1 bidirectional soft composite bending actuator and **c** images from $t = 0$ s to $t = 8$ s showing bidirectional bending motions. **d** Timing of input currents to each SMA wire from $t = 0$ s to $t = 8$ s

3.3 Multi-mode, Bidirectional Soft Composite Bending Actuator

We next fabricated an actuator with more combinations of distinct interwoven SMA wire patterns within the glass fiber textile; this actuator exhibited multi-mode bidirectional bending. As shown in Fig. 15(a, b), the actuator contains four interwoven SMA wires with Type-1 and -2 weaving patterns: two outer/inner Type-1/-2 SMA wires in reversed orientations (SMA wires 1, 2/3, 4) for the first/second bidirectional bending motions. Upon actuation of wires 1 and 2, the actuator bends in the first mode; the two (opposite) orientations of the Type-1 wires control the bending direction. Actuation of the inner wires (3 and 4) deforms the actuator in the second bending mode; the two (opposite) orientations of the wires control the bending direction. Figure 15(c) captures the multi-mode bidirectional bending motions induced by sequential activations of each wire from $t = 0$ s to $t = 8$ s. A 500-mA step current was sequentially applied to each SMA wire over this interval (1-s activation times, during which the inputs to other wires were zero). The timing diagram is shown in Fig. 15(d).

Supplementary Movie S5 captures the motions of the actuator depicted in Fig. 15(c). Many similar actuators in

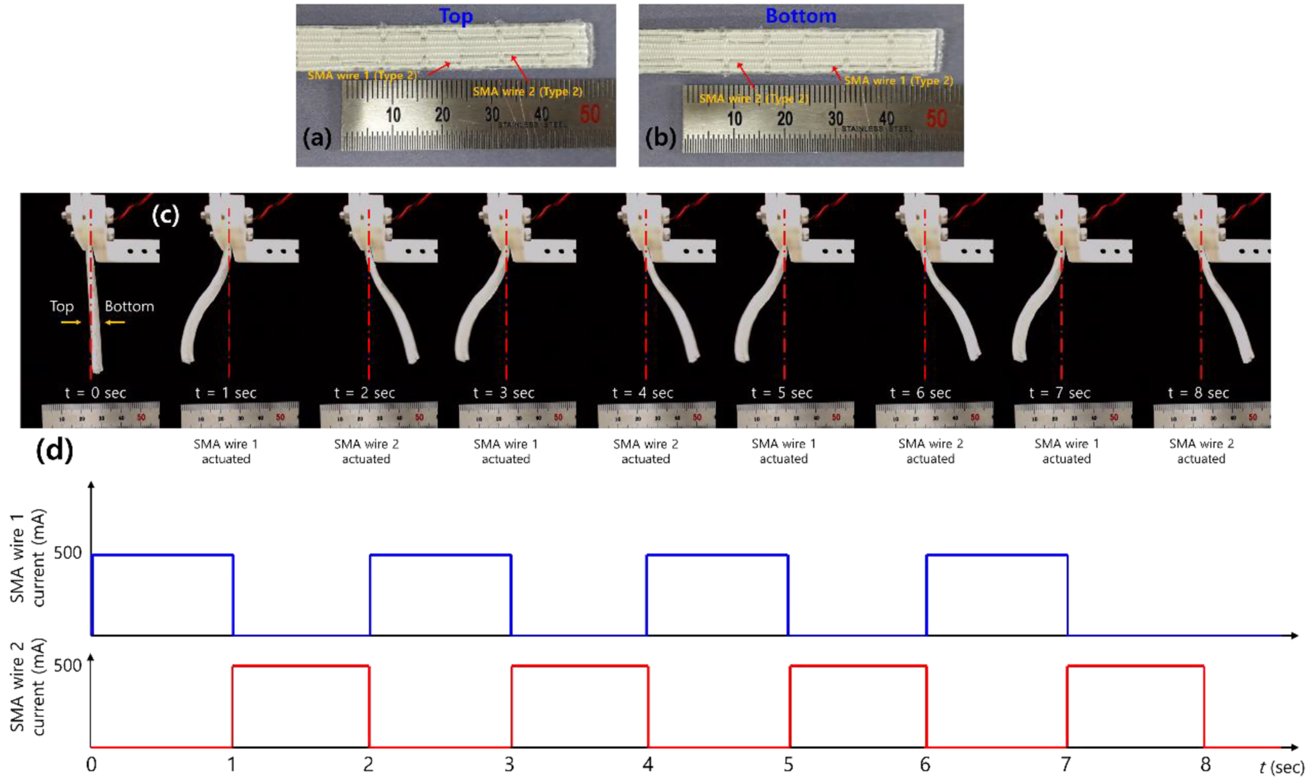

Fig. 14 **a**, **b** Optical images of a Type-2 bidirectional soft composite bending actuator and **c** images from $t=0$ s to $t=8$ s showing bidirectional bending motions. **d** Timing of sequential input currents to each SMA wire from $t=0$ s to $t=8$ s

earlier studies focused on specific applications using single actuation modes [19, 25, 34, 38, 39]. The combined motions suggest that our actuator will have applications in soft robotics and associated fields that require complicated flexible motions.

3.4 Soft Grippers Based on multi-mode soft Composite Bending Actuators

We prepared two soft grippers each with four soft actuators that differed in terms of their bending modes. The first soft gripper was fabricated by configuration of four Type-1 actuators [Supplementary Figure S6(a)]; the second soft gripper was fabricated by configuration of four Type-2 actuators [Supplementary Figure S6(b)]. The motions upon independent actuation of each finger of the soft grippers are shown in Supplementary Figure S6(a, b); the actuated fingers are denoted by red arrows. The 500-mA step current was applied to each wire for several seconds. Supplementary Movie S6 shows the motions of the grippers depicted in Supplementary Figure S6(a, b). The two soft grippers exhibit different gripping motions that can be adjusted according to object size and shape. We next studied the gripping motions of three soft grippers each with four Type-1, -2, and -3 actuators. Figure 16(a–c) show the gripping motions. In Fig. 16(a), a gripper with Type-1 actuators grasps an object of mass 28.9 g by surrounding nearly the entire surface of the object. We simultaneously applied 500 mA to all four actuators. Figure 16(b) shows that the second gripper (with Type-2 actuators) grips an object of mass 4.5 g in a tweezers-like manner, which involves less surface contact, upon the simultaneous application of 500 mA to all four Type-2 actuators. Although the object in Fig. 16(b) is lighter than the object in Fig. 16(a), the small contact area would minimize damage

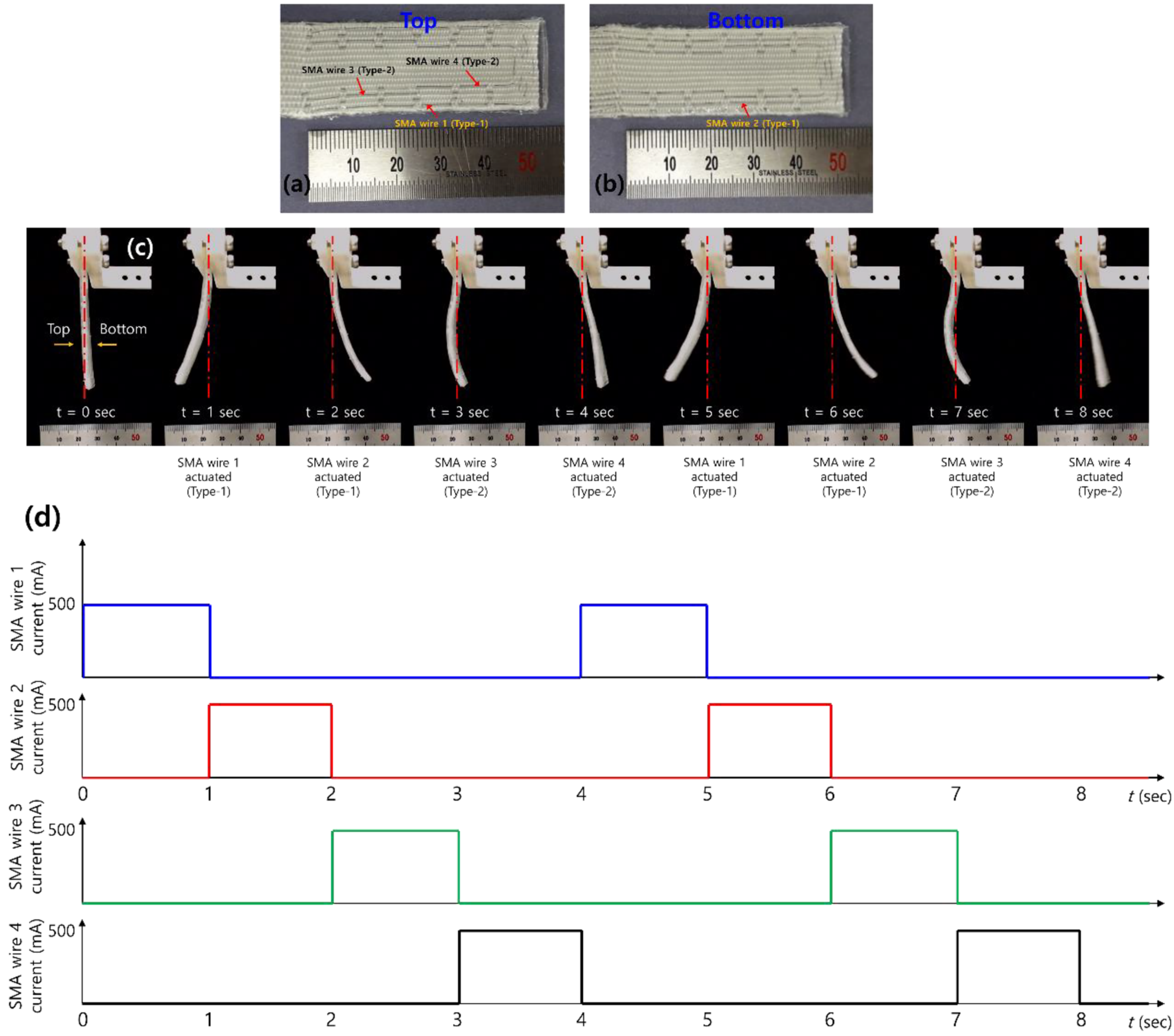

Fig. 15 **a**, **b** Optical images of a multi-mode and bidirectional (Type-1 and -2) soft composite bending actuator and **c** images captured from $t=0$ s to $t=8$ s showing multi-mode bidirectional bending motions. **d** Timing of sequential input currents to each SMA wire from $t=0$ s to $t=8$ s

to an object that is weak or sensitive to external stimuli. Figure 16(c) shows a gripper with four Type-3 actuators, along with the gripping motions; 500 mA was simultaneously applied to all four actuators. This gripper prototype holds a flat object of mass 6.8 g by surrounding the exterior of the object; the gripper holds flat objects more effectively compared with a gripper that exhibits Type-1 actuations. The simple demonstrations in Fig. 16(a–c) demonstrate proof of concept; the multi-mode actuators are adaptable. Similar grippers were reported in previous works, but they generally focused on specific applications that used a single actuation mode; the adjustable gripping motions in the present study create more complicated and flexible motions. The proposed soft composite actuator will be potentially useful in soft grippers [44, 45], robotics [46–49], flapping actuators [50], and other related engineering applications. Supplementary

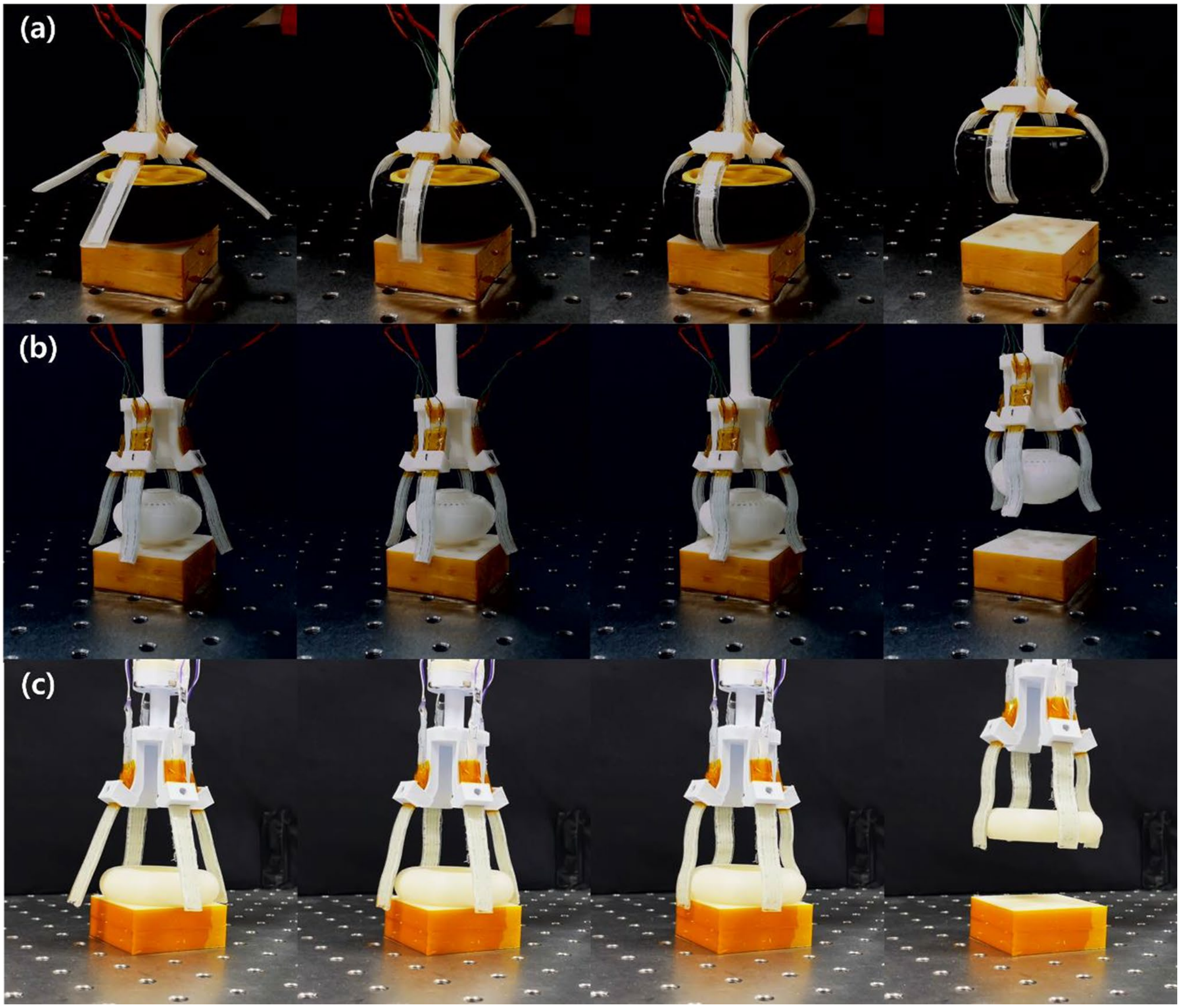

Fig. 16 Motions of the grippers with four **a** Type-1, **b** Type-2, and **c** Type-3 soft composite bending actuators

Movie S7 captures the motions of the grippers depicted in Fig. 16(a–c).

4 Conclusion

We present multi-mode soft composite bending actuators fabricated from glass fiber textiles interwoven with SMA wires, along with a soft matrix (PDMS). We explored Type-1, -2, and -3 bending modes in terms of bending deformation (curvature), stiffness (grade) of glass fiber textile, and diameter of SMA wire. The maximum mean bending curvatures were 0.079, 0.091, and 0.11 mm^{-1} for Type-1, -2, and -3 actuators, respectively, when 500 mA was applied. We extended our work to bidirectional multi-mode actuators; we combined different SMA wire interweavings in similar glass fiber textiles. We present examples of such actuators and describe their complex motions. Finally, we fabricated soft grippers using Type-1, -2, and -3 actuators; we describe their gripping motions. Our key contributions are: (1) the detailed design and fabrication of multi-mode soft composite bending actuators; (2) the induction and control of complex actuator motions; and (3) the construction of soft grippers and a discussion of their potential applications. Our work will advance the field of soft robotics and will be useful in other scientific and engineering applications.

4.1 Materials

The glass fiber yarn (EC D450, CPIC) used to prepare the woven textile threads (T20 and T40) and the SMA wire (100- and 150-μm diameter Flexinol SMA wire, phase transition temperature 70 °C; Dynalloy Inc.) were used as purchased. The soft matrix was prepared using PDMS (Sylgard 184, Dow Corning) and a curing agent; the PDMS:curing agent mass ratio was 20:1 for all specimens. All specimens were cured at room temperature for 24 h.

Supplementary Information The online version contains supplementary material available at https://doi.org/10.1007/s40684-022-00491-3.

Acknowledgements This work was supported by the grant funded by Ministry of Trade, Industry and Energy (MOTIE, Korea) and the Korea Evaluation Institute of Industrial Technology (KEIT) (Grant No. 20006388, and No. 20017462); and the National Research Foundation of Korea (NRF) grant funded by the Korea government (MSIT) (No. NRF-2020R1A2C4001731).

Author Contributions G-YL conceptualized this work. G-YL and OT designed the materials and specimens. G-YL and G-SL designed the experiments and set the experimental setups. OT and G-YL fabricated the specimens. G-YL, OT, G-SL conducted the experiments. G-YL and OT analyzed the data and wrote the paper, and all authors provided feedback. G-YL supervised the project.

Declarations

Conflict of interest The authors declare that they have no conflict of interest.

References

1. Kim, S., Laschi, C., & Trimmer, B. (2013). Soft robotics: a bioinspired evolution in robotics. *Trends Biotechnol*, *31*(5), 287–294. https://doi.org/10.1016/j.tibtech.2013.03.002.
2. Rus, D., & Tolley, M. T. (2015). Design, fabrication and control of soft robots. *Nature*, *521*(7553), 467–475. https://doi.org/10.1038/nature14543.
3. Mirvakili, S. M., & Hunter, I. W. (2018). Artificial muscles: mechanisms, applications, and Challenges. *Advanced materials*, *30*(6), 1704407. https://doi.org/10.1002/adma.201704407.
4. Mohd Jani, J., Leary, M., Subic, A., & Gibson, M. A. (2014). A review of shape memory alloy research, applications and opportunities. *Materials & Design (1980–2015)*, 56, 1078–1113. https://doi.org/10.1016/j.matdes.2013.11.084
5. Han, M. W., Rodrigue, H., Cho, S., Song, S. H., Wang, W., Chu, W. S., & Ahn, S. H. (2016). Woven type smart soft composite for soft morphing car spoiler. *Composites Part B: Engineering*, *86*, 285–298. https://doi.org/10.1016/j.compositesb.2015.10.009.
6. Jeong, J., Yasir, I. B., Han, J., Park, C. H., Bok, S. K., & Kyung, K. U. (2019). Design of shape memory alloy-based Soft Wearable Robot for assisting wrist motion. *Applied Sciences*, *9*(19), 4025. https://doi.org/10.3390/app9194025.
7. Lee, S., Lee, S., Na, Y., Ahn, B., Jung, H., Cheng, S. S., Kim, N., Jun, T. S., & Kim, Y. (2019). Shock absorber mechanism based on an SMA spring for Lightweight Exoskeleton Applications. *International Journal of Precision Engineering and Manufacturing*, *20*(9), 1533–1541. https://doi.org/10.1007/s12541-019-00169-y.
8. Zainal, M., Sahlan, S., & Ali, M. (2015). Micromachined shape-memory-alloy microactuators and their application in Biomedical Devices. *Micromachines*, *6*(7), 879–901. https://doi.org/10.3390/mi6070879.
9. Akbari, S., Sakhaei, A. H., Panjwani, S., Kowsari, K., & Ge, Q. (2021). Shape memory alloy based 3D printed composite actuators with variable stiffness and large reversible deformation. *Sensors and Actuators A: Physical*, *321*, 112598. https://doi.org/10.1016/j.sna.2021.112598.
10. Akbari, S., Sakhaei, A. H., Panjwani, S., Kowsari, K., Serjouei, A., & Ge, Q. (2019). Multimaterial 3D printed soft actuators powered by shape memory alloy wires. *Sensors and Actuators A: Physical*, *290*, 177–189. https://doi.org/10.1016/j.sna.2019.03.015.
11. Du, Y., Liu, B., Xu, M., Dong, E., Zhang, S., & Yang, J. (2015). Dynamic characteristics of planar bending actuator embedded with shape memory alloy. *Mechatronics*, *25*, 18–26. https://doi.org/10.1016/j.mechatronics.2014.11.001.
12. Kim, H. I., Han, M. W., Song, S. H., & Ahn, S. H. (2016). Soft morphing hand driven by SMA tendon wire. *Composites Part B: Engineering*, *105*, 138–148. https://doi.org/10.1016/j.compositesb.2016.09.004.
13. Li, J., Zu, L., Zhong, G., He, M., Yin, H., & Tan, Y. (2017). Stiffness characteristics of soft finger with embedded SMA fibers. *Composite Structures*, *160*, 758–764. https://doi.org/10.1016/j.compstruct.2016.10.045.
14. Costanza, G., & Tata, M. E. (2020). Shape memory alloys for Aerospace, recent developments, and New Applications: a short review. *Materials (Basel)*, *13*(8), 1856. https://doi.org/10.3390/ma13081856.
15. Han, M. W., Rodrigue, H., Kim, H. I., Song, S. H., & Ahn, S. H. (2016). Shape memory alloy/glass fiber woven composite for soft morphing winglets of unmanned aerial vehicles. *Composite Structures*, *140*, 202–212. https://doi.org/10.1016/j.compstruct.2015.12.051.
16. Lee, S. H., & Kim, S. W. (2020). Self-sensing-based deflection control of carbon fibre-reinforced polymer (CFRP)-based shape memory alloy hybrid composite beams. *Composite Structures*, *251*, 112544. https://doi.org/10.1016/j.compstruct.2020.112544.
17. Shim, J. E., Quan, Y. J., Wang, W., Rodrigue, H., Song, S. H., & Ahn, S. H. (2015). A smart soft actuator using a single shape memory alloy for twisting actuation. *Smart Materials and Structures*, *24*(12), 125033. https://doi.org/10.1088/0964-1726/24/12/125033.
18. Lohse, F., Kopelmann, K., Grellmann, H., Ashir, M., Gereke, T., Hantzsche, E., Sennewald, C., & Cherif, C. (2022). Experimental and Numerical Analysis of the deformation behavior of Adaptive Fiber-Rubber Composites with Integrated shape memory alloys. *Materials (Basel)*, *15*(2), 582. https://doi.org/10.3390/ma15020582.
19. Smith, C., Villanueva, A., Joshi, K., Tadesse, Y., & Priya, S. (2011). Working principle of bio-inspired shape memory alloy composite actuators. *Smart Materials and Structures*, *20*(1), 012001. https://doi.org/10.1088/0964-1726/20/1/012001.
20. Ashir, M., & Cherif, C. (2020). Development of shape memory alloy-based adaptive fiber-reinforced plastics by means of open reed weaving technology. *Journal of Reinforced Plastics and Composites*, *39*(15–16), 563–571. https://doi.org/10.1177/0731684420920941.
21. Ashir, M., Vorhof, M., & Nocke, A. (2019). Influence of thickness ratio and integrated weft yarn column numbers in shape memory alloys on the deformation behavior of adaptive fiber-reinforced plastics. *Composite Structures*, *215*, 493–501. https://doi.org/10.1016/j.compstruct.2019.02.081.
22. Fu, C., Xia, Z., Hurren, C., Nilghaz, A., & Wang, X. (2022). Textiles in soft robots: current progress and future trends. *Biosensors & Bioelectronics*, *196*, 113690. https://doi.org/10.1016/j.bios.2021.113690.
23. Ke, J., Gao, J., Wu, Z., Xiang, Z., & Hu, X. (2022). Vari-stiffness characteristics of a 3D SMA hybrid basalt woven composite. *Composite Structures*, *285*, 115192. https://doi.org/10.1016/j.compstruct.2022.115192.

24. Song, S. H., Lee, J. Y., Rodrigue, H., Choi, I. S., Kang, Y. J., & Ahn, S. H. (2016). 35 hz shape memory alloy actuator with bending-twisting mode. *Scientific reports*, *6*, 21118. https://doi.org/10.1038/srep21118.
25. Lee, J. H., Chung, Y. S., & Rodrigue, H. (2019). Long shape memory Alloy Tendon-based Soft robotic actuators and implementation as a soft gripper. *Scientific reports*, *9*(1), 11251. https://doi.org/10.1038/s41598-019-47794-1.
26. Rodrigue, H., Wang, W., Bhandari, B., Han, M. W., & Ahn, S. H. (2015). SMA-based smart soft composite structure capable of multiple modes of actuation. *Composites Part B: Engineering*, *82*, 152–158. https://doi.org/10.1016/j.compositesb.2015.08.020.
27. Wu, R., Han, M. W., Lee, G. Y., & Ahn, S. H. (2013). Woven type smart soft composite beam with in-plane shape retention. *Smart Materials and Structures*, *22*(12), 125007. https://doi.org/10.1088/0964-1726/22/12/125007.
28. Rodrigue, H., Wang, W., Kim, D. R., & Ahn, S. H. (2017). Curved shape memory alloy-based soft actuators and application to soft gripper. *Composite Structures*, *176*, 398–406. https://doi.org/10.1016/j.compstruct.2017.05.056.
29. She, Y., Li, C., Cleary, J., & Su, H. J. (2015). Design and fabrication of a Soft Robotic Hand with embedded actuators and sensors. *Journal of Mechanisms and Robotics*, *7*(2), 021007. https://doi.org/10.1115/1.4029497.
30. Shintake, J., Cacucciolo, V., Floreano, D., & Shea, H. (2018). Soft robotic grippers. *Advanced materials*, *30*(29), 1707035. https://doi.org/10.1002/adma.201707035.
31. Wang, W., & Ahn, S. H. (2017). Shape memory alloy-based soft gripper with variable stiffness for compliant and effective grasping. *Soft robotics*, *4*(4), 379–389. https://doi.org/10.1089/soro.2016.0081.
32. Wang, W., Rodrigue, H., Kim, H. I., Han, M. W., & Ahn, S. H. (2016). Soft composite hinge actuator and application to compliant robotic gripper. *Composites Part B: Engineering*, *98*, 397–405. https://doi.org/10.1016/j.compositesb.2016.05.030.
33. Wang, W., Tang, Y., & Li, C. (2021). Controlling bending deformation of a shape memory alloy-based soft planar gripper to grip deformable objects. *International Journal of Mechanical Sciences*, *193*, 106181. https://doi.org/10.1016/j.ijmecsci.2020.106181.
34. Han, M. W., Kim, M. S., & Ahn, S. H. (2020). Shape memory textile composites with multi–mode actuations for soft morphing skins. *Composites Part B: Engineering*, *198*, 108170. https://doi.org/10.1016/j.compositesb.2020.108170.
35. Sharma, A. K., Bhandari, R., Aherwar, A., & Rimašauskienė, R. (2020). Matrix materials used in composites: A comprehensive study. *Materials Today: Proceedings*, 21, 1559–1562. https://doi.org/10.1016/j.matpr.2019.11.086
36. Nespoli, A., Besseghini, S., Pittaccio, S., Villa, E., & Viscuso, S. (2010). The high potential of shape memory alloys in developing miniature mechanical devices: a review on shape memory alloy mini-actuators. *Sensors and Actuators A: Physical*, *158*(1), 149–160. https://doi.org/10.1016/j.sna.2009.12.020.
37. Bekker, A., & Brinson, L. C. (1997). Temperature-induced phase transformation in a shape memory alloy: phase diagram based kinetics approach. *Journal of the Mechanics and Physics of Solids*, *45*(6), 949–988. https://doi.org/10.1016/S0022-5096(96)00111-1.
38. Lalegani Dezaki, M., Bodaghi, M., Serjouei, A., Afazov, S., & Zolfagharian, A. (2022). Adaptive reversible composite-based shape memory alloy soft actuators. *Sensors and Actuators A: Physical*, *345*, 113779. https://doi.org/10.1016/j.sna.2022.113779.
39. Mersch, J., Bruns, M., Nocke, A., Cherif, C., & Gerlach, G. (2021). High-Displacement, Fiber-Reinforced shape memory Alloy Soft Actuator with Integrated Sensors and its Equivalent Network Model. *Advanced Intelligent Systems*, *3*(7), 2000221. https://doi.org/10.1002/aisy.202000221.
40. Leary, M., Huang, S., Ataalla, T., Baxter, A., & Subic, A. (2013). Design of shape memory alloy actuators for direct power by an automotive battery. *Materials & Design*, *43*, 460–466. https://doi.org/10.1016/j.matdes.2012.07.002.
41. Furst, S. J., & Seelecke, S. (2012). Modeling and experimental characterization of the stress, strain, and resistance of shape memory alloy actuator wires with controlled power input. *Journal of Intelligent Material Systems and Structures*, *23*(11), 1233–1247. https://doi.org/10.1177/1045389x12445036.
42. Dana, A., Vollach, S., & Shilo, D. (2021). Use the force: review of high-rate actuation of shape memory alloys. *Actuators*, *10*(7), 140. https://doi.org/10.3390/act10070140.
43. Jeong, S., & Yoo, H. H. (2017). Flexibility modeling of a beam undergoing large deflection using the assumed mode method. *International Journal of Mechanical Sciences*, *133*, 611–618. https://doi.org/10.1016/j.ijmecsci.2017.08.059.
44. Shin, J. H., Park, J. G., Kim, D. I., Yoon, H. S. (2021). A universal soft gripper with the optimized fin ray finger. *International Journal of Precision Engineering and Manufacturing-Green Technology*, *8*(3), 889–899. https://doi.org/10.1007/s40684-021-00348-1
45. Gwon, M., Park, G., Hong, D., Park, Y-J., Han, S., Kang, D., Koh, J. (2022). Soft directional adhesion gripper fabricated by 3D printing process for gripping flexible printed circuit boards. *International Journal of Precision Engineering and Manufacturing-Green Technology*, *9*(4), 1151–1163. https://doi.org/10.1007/s40684-021-00368-x
46. Huang, X., Ford, M., Patterson, Z. J., Zarepoor, M., Pan, C., Majidi, C. (2020). Shape memory materials for electrically-powered soft machines. *Journal of Materials Chemistry B*, *8*(21), 4539–4551. https://doi.org/10.1039/D0TB00392A
47. Park, S., Koh, D., Shim, J., Kim, J.-J., Lee, S.-K. (2021). Gantry type lapping manipulator toward unmanned lapping process for a large work surface. *International Journal of Precision Engineering and Manufacturing-Green Technology*, *8*(6), 1723–1737. https://doi.org/10.1007/s40684-020-00274-8
48. Rus, D., Tolley, M. T. (2015). Design fabrication and control of soft robots. *Nature*, *521*(7553), 467–475. https://doi.org/10.1038/nature14543
49. Pham, A.-D., Ahn, H.-J. (2021). Rigid precision reducers for machining industrial robots. *International Journal of Precision Engineering and Manufacturing*, *22*(8), 1469–1486. https://doi.org/10.1007/s12541-021-00552-8
50. Lee, C., Kim, S., Chu, B. (2021). A survey: flight mechanism and mechanical structure of the UAV. *International Journal of Precision Engineering and Manufacturing*, *22*(4), 719–743. https://doi.org/10.1007/s12541-021-00489-y

Oybek Valijonovich Tuyboyov is currently a Ph.D. candidate in the department of Mechanical Engineering at Kumoh National Institute of Technology. He received a B.S. degree in 2009 and a M.Sc. degree in 2011 in Mechanical Engineering from Tashkent State Technical University. His research interests include soft robotics, actuators, manufacturing process, and product design.

Geo-Sung Lee is currently a postmaster researcher in the department of Mechanical Engineering at Kumoh National Institute of Technology. He received a B.S. degree in 2020 and a M.S. degree in 2022 in Mechanical Engineering from Kumoh National Institute of Technology. His research interests include smart materials/structures, product design, and additive manufacturing.

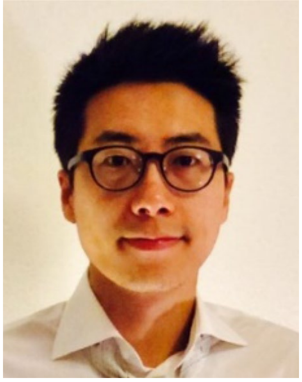

Gil-Yong Lee received a Ph.D. degree in Mechanical and Aerospace Engineering from Seoul National University in 2013. He has been affiliated with Seoul National University, and University of Washington. He is currently an assistant professor in the department of Mechanical Engineering at Kumoh National Institute of Technology. His research interests include integrated manufacturing system, sensors/actuators, composites, micro/nano fabrications, vibration, control, and additive manufacturing.